ORIGINAL ARTICLE

lajss.org
Latin American Journal of Solids and Structures

www.lajss.org

Scattering of Plane SV Waves by Underwater Tunnel

Jia Ha[a], Guochao Li[a*], Mingjian Yu[a], Chong Niu[a], Yanjun Fan[a]

[a]Yellow River Engineering Consulting Co., Ltd., Zhengzhou 450003, China. Email: 29119270@qq.com, algcycg@163.com, 18695801153@163.com, 490844337@qq.com, 273963468@qq.com

*Corresponding author

https://doi.org/10.1590/1679-7825/e8382

Abstract

Accounting for fluid-solid coupling in saturated underwater soils, the scattering problem of underwater tunnel under plane SV-wave incidence is investigated by using the Fourier-Bessel series expansion method of wave function. Numerical examples analyze the effects of incident wave angle, frequency, tunnel burial depth, and porosity on displacement at the water-soil interface and dynamic stress concentration on the tunnel surface. When η=0.5, increasing the incident angle reduces horizontal displacement by up to 39.3%, increases vertical displacement by up to 96.2%, and raises the Dynamic Stress Concentration Factor (DSCF) on the tunnel surface by 65.6%. Porosity shows minimal impact on stress and displacement. As porosity increases, horizontal displacement decreases by up to 2.1%, vertical displacement increases by approximately 1.23%, and DSCF decreases by 1.2%. As incident frequency increases, displacement and stress distributions become more complex, with more pronounced peaks, and troughs. Maximum horizontal displacement increases by 86.4%, and vertical displacement by 91.2%. Displacement and stress concentration are most pronounced above the tunnel under shallow burial conditions.

Keywords

Saturated soil; Underwater tunnel; Scattering; Plane SV wave

Graphical Abstract

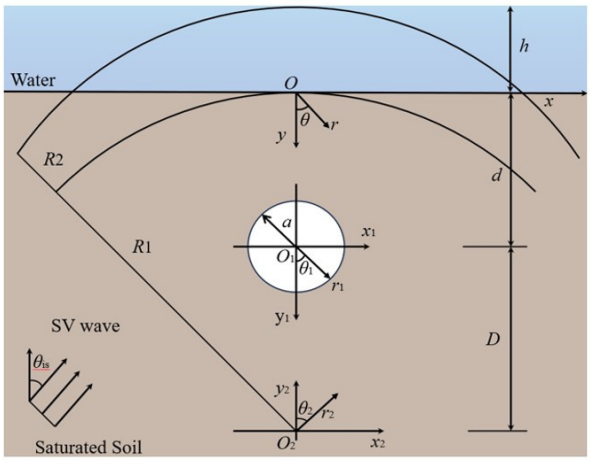

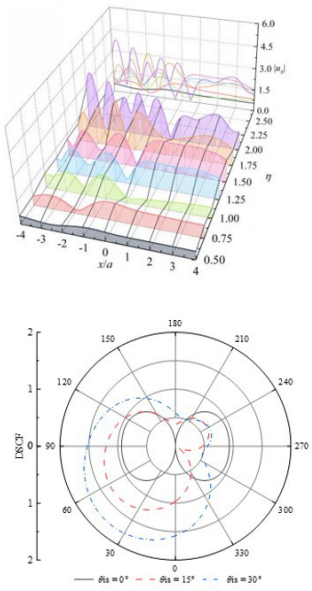

Received: set. 26, 2024. In revised form: out. 28, 2024. Accepted: out. 31, 2024. Available online: nov. 04, 2024
https://doi.org/10.1590/1679-7825/e8382

1 INTRODUCTION

The rapid growth of marine engineering and the expansion of critical underwater infrastructures, such as subsea tunnels and submarine gas pipelines, have led to in-creased construction in seafloor sediments, raising concerns about seismic activity in these environments. Underwater tunnels serve as crucial hubs for transportation and logistics, possessing significant economic and social value. However, the safety of underwater tunnels under seismic forces is directly related to the safety of lives and property. If the tunnel is damaged by an earthquake, it could result in significant eco-nomic loss and potentially catastrophic consequences. The core of research into the seismic response of underwater tunnels lies in exploring the scattering effects of seismic waves, particularly their propagation mechanisms in complex geological structures and under the coverage of seawater.

The study of plane wave scattering around tunnels has attracted considerable attention from scholars both at home and abroad, laying a crucial foundation for exploring the seismic response mechanism of land-based tunnels. Pao et al. (1973) first applied the wave function expansion method to investigate dynamic stress concentration caused by elastic wave incidence in an infinite space with a cavity. Lee and Trifunac (1970) later extended the study to half-space and derived a solution for SH wave incidence on a half-space cavity. Cao and Lee (1979), Lee and Cao (1989), along with Todorovska (1990), Todorovska and Lee (1991), explored the scattering effects of P, SV, and Rayleigh waves under concave terrain using the large circular arc assumption. Davis et al. (2001) derived an analytical solution for SV wave scattering around underground cavities and pipelines. Liang et al. (2003, 2004, 2005) derived analytical solutions for scattered waves around single tunnels, twin tunnels, and tunnel groups in single-phase half-space. Zhang et al. (2022) derives an analytical solution for the dynamic response of a circular lined tunnel under plane SH wave scattering, revealing the mechanism by which a partially imperfect interface affects the stress and displacement fields in tunnel linings. Liang et al. (2023) propose a complex function solution for the scattering of plane SH waves by circular tunnels in a nonlocal fractional-order viscoelastic half-space. Zhao et al. (2023a) present a semi-analytical solution for the 3D scattering of plane harmonic waves by a cylindrical tunnel in an elastic half-space.

Traditional elastic wave theory, based on single-phase solid media. To accurately simulate seismic wave propagation in saturated sites, the interaction of multiphase media in the soil must be considered. Scholars have made significant progress in studying wave propagation in two-phase saturated media based on Biot's poroelastic theory (Biot., 1956a, 1956b). Zimmerman and Stern (1993) applied Biot wave theory to investigate wave scattering in porous media, while Senjuntichai and Rajapakse (1993) focused on wave interactions with sealed circular cavities in a full-space environment. Both Liang et al. (2007a, 2007b), along with Li and Zhao (2004, 2008), employed the wave function expansion method to solve scattering problems of P-waves and SV waves in saturated soil half-space, focusing on unlined and circular cavities, respectively. Xu et al. (2019) derived an analytical solution for the scattering of plane P-waves around a single-layer lined tunnel. Liu et al. (2024) solve the SV-wave scattering problem for convex circular topography with seawater and an underlying tunnel in a saturated half-space. Zhu et al. (2024) and Yuan et al. (2024) investigate ground motion amplification and vibrations induced by twin tunnels in saturated poroelastic soil, utilizing both numerical and analytical models to analyze seismic wave responses. Liu et al. (2021a) and Huang et al. (2022) used the indirect boundary element method and boundary integral equation method to solve seismic wave diffraction problems in fluid-saturated and three-dimensional layered half-spaces.

The seawater adds complexity to the seismic response of underwater sites compared to land-based locations. Feng et al. (2023) used numerical methods to solve the scattering problem of plane SV waves in a semicircular canyon with a water layer. Liu et al. (2021b, 2023) investigated P-wave scattering in arc-shaped sites with water-saturated biphasic media and V-shaped canyons with partial water coverage. These studies show that a water layer significantly influences seismic ground motion characteristics at local terrain sites. Research on elastic wave scattering by tunnels in underwater soils remains limited. Analyzing SV wave scattering helps simulate the forces and damage mechanisms exerted by seismic waves on tunnels and other long linear structures. This provides critical theoretical support for seismic design of underwater tunnels and offers reference value for the safety design of subsea tunnels and seismic response analysis in complex sites.

Current seismic analysis of tunnel structures in aquatic environments mainly examines wave scattering in tunnels without overlying water, limiting its relevance to real-world scenarios involving water saturation. Seismic response research is needed for water-covered, non-planar, two-phase medium sites. The dynamic interaction between water, saturated soil, and the structure is considered, accounting for wave reflection, absorption by the water layer, and the fluid-solid coupling of the underwater soil. The water layer is modeled as an ideal fluid, and the underwater soil as a saturated porous medium. Using fluid wave theory and Biot's saturated porous medium theory, the Fourier-Bessel series method provides an analytical solution for the scattering of plane SV waves around an unlined underwater tunnel. Numerical simulations analyze how incident angle, wave frequency, tunnel depth, and porosity affect horizontal and

vertical displacements, and the dynamic stress concentration factor (DSCF) at the water-soil interface and tunnel surface. This study uncovers the fluid-solid coupling mechanisms in the water-soil-structure system during seismic events, offering theoretical support for the seismic design of underwater tunnels.

2 Model and basic equations

The underwater soil layer is modeled as a saturated porous medium, with the analytical model depicted in Figure 1. This model consists of a tunnel, saturated soil, and a seawater layer. The tunnel is located within the saturated soil layer. The site model adopts Cartesian coordinate systems (x, y), (x_1, y_1), (x_2, y_2), and cylindrical coordinate systems (r_1, ϑ_1), (r_2, ϑ_2). The tunnel has a radius "a" and depth "d," with the seawater layer thickness "h" and the tunnel's center at point O_1. It is assumed that the seawater layer in the model is an ideal fluid medium, and the saturated soil layer is a two-phase saturated porous medium.

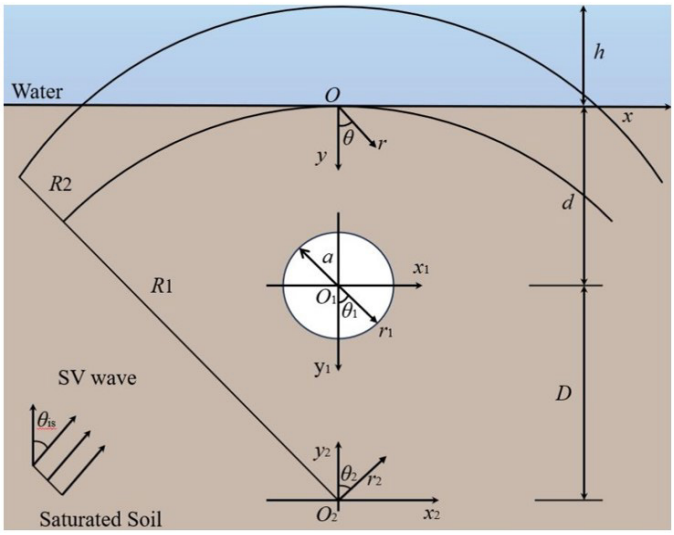

Figure 1 Site model.

The constitutive and motion equations for the fluid are as follows (Wang., 1984):

$$-P_W = K_W \nabla \cdot \boldsymbol{U}_W \tag{1}$$

$$K_W \nabla \nabla \cdot \boldsymbol{U}_W = \rho_W \ddot{\boldsymbol{U}}_W \tag{2}$$

where P_W denotes the hydrodynamic pressure; K_W represents the bulk modulus; ρ_W is the density of water; $\boldsymbol{U}_W$ represents the displacement vector of water.

The displacement vector $\boldsymbol{U}_W$ of the water layer can be expressed using the potential function φ_W, as follows:

$$\boldsymbol{U}_W = \nabla \varphi_W \tag{3}$$

The Eqs. (1) and (2) are expressed by potential functions as:

$$-P_W = K_W \nabla^2 \varphi_W \tag{4}$$

$$K_W \nabla^2 \varphi_W = \rho_W \ddot{\varphi}_W^2 \tag{5}$$

The P-wave velocity and wavenumber in the water layer are expressed as follows:

$$c_W = \sqrt{K_W / \rho_W} \tag{6}$$

$$k_W = 2\pi f \sqrt{\rho_W / K_W} \tag{7}$$

The underwater soil layer is modeled as saturated soil, with the following assumptions: (1) The soil skeleton is an elastic, porous medium, and the soil particles are incompressible; (2) The pore water is a compressible ideal fluid, flowing through the soil according to Darcy's law; (3) The soil is statistically isotropic, with uniformly distributed, interconnected pores; (4) A coupling effect exists between adjacent phases; (5) Seepage force accounts for both viscous forces in the pore water and resistance from the tortuous pore channels; (6) Temperature and other effects on the wave equation are temporarily ignored.

Based on Biot's theory, the fundamental equations for saturated porous media are as follows (Zhou et al., 2013):

Physics equations:

$$\sigma_{ij} = 2\mu\varepsilon_{ij} + (\lambda\varepsilon_{kk} - \alpha p)\delta_{ij},\ \zeta = \alpha\varepsilon_{kk} + \frac{1}{M}p \tag{8}$$

Geometric equation:

$$\varepsilon_{ij} = \frac{1}{2}(u_{i,j} + u_{j,i}) \tag{9}$$

Motion equation:

$$\sigma_{ij,j} = \rho\ddot{u}_i^{\mathrm{s}} + \rho_{\mathrm{f}}\ddot{u}_i^{\mathrm{f}},\ -p_{,i} = \rho_{\mathrm{f}}\ddot{u}_i^{\mathrm{s}} + m\ddot{u}_i^{\mathrm{f}} + b\dot{u}_i^{\mathrm{f}} \tag{10}$$

where: $\sigma_{ij,j}$ and p denote the total stress component of the saturated porous medium and the pore fluid pressure, respectively; $\zeta = -u_{i,i}^{\mathrm{f}}$ and $\theta = u_{j,j}^{\mathrm{s}}$ (i, j = 1, 2, 3); $u^{\iota}(\iota = \mathrm{s}、\ \mathrm{f})$ represents the displacement of the solid skeleton and the relative displacement of the fluid. ι is used to define the respective components of the saturated soil. λ and μ are Lamé constants; $b = \eta_{\mathrm{b}} / k_{\mathrm{f}}$, where η_{b} is the fluid viscosity coefficient of the saturated soil, and k_{f} represents the permeability coefficient. α and M are Biot parameters representing material compressibility, where $\alpha = 1 - K_{\mathrm{b}}/K^{\mathrm{s}}$, and $1 / M = (\alpha - n) / K^{\mathrm{s}} + n / K^{\mathrm{f}}$. n is the porosity. K_{b} is the bulk modulus of the solid skeleton, K^{s} is the bulk modulus of the solid particles, and K^{f} is the bulk modulus of the pore fluid. $m = \rho^{\mathrm{f}} / n$ represents a parameter related to the mass density of pore water and the geometric characteristics of the pores; $\rho = (1-n)\rho^{\mathrm{s}} + n\ \rho^{\mathrm{f}}$ represents the mass density of the mixture, and ρ^{s} and ρ^{f} represent the densities of the solid and liquid phases, respectively.

The governing equation for the dynamic response of saturated soil is derived from Equations (8) to (10):

$$\mu\nabla^2 u^{\mathrm{s}} + \mathrm{grad}[(\mu\ + \lambda\ + \alpha^2 M)\theta] - \mathrm{grad}(\alpha M\zeta) = \rho\ \ddot{u}^{\mathrm{s}} + \rho^{\mathrm{f}}\ddot{u}^{\mathrm{f}} \tag{11}$$

$$K_W\nabla^2\varphi_W = \rho_W\ddot{\varphi}_W^2 \tag{12}$$

Based on the Helmholtz vector decomposition theorem, the displacement vector in saturated soil can be expressed as:

$$\begin{aligned} u^{\mathrm{s}} &= \nabla\varphi_{\mathrm{s}} + \nabla\times\boldsymbol{\psi}_{\mathrm{s}} \\ u^{\mathrm{f}} &= \nabla\varphi_{\mathrm{f}} + \nabla\times\boldsymbol{\psi}_{\mathrm{f}} \end{aligned} \tag{13}$$

When SV wave is incident, with circular frequency ω and incident angle ϑ_{is}, the incident wave can be expressed as:

$$\boldsymbol{\psi}_{\mathrm{is}}^{\iota}\left(x,\ y\right) = B_{\mathrm{is}}^{\iota}\exp\left[\mathrm{i}k_{\mathrm{is}}\left(x\sin\theta_{\mathrm{is}} - y\cos\theta_{\mathrm{is}}\right) - \mathrm{i}\omega t\right] \tag{14}$$

where k_{is} is the wave number of SV wave. $\exp(\mathrm{i}\omega t)$ is left out for simplicity, the above equations could be expressed as:

$$\varphi_{\mathrm{i}}^{\iota}\left(x,y\right) = A_{\mathrm{ip1}}^{\iota}\exp[\mathrm{i}k_{\mathrm{ip1}}(x\sin\theta_{\mathrm{ip1}} - y\cos\theta_{\mathrm{ip1}})] \tag{15}$$

The SV wave generates reflected P_1, P_2, and SV waves at the water-soil interface, along with transmitted and reflected P waves in the water. The wave potential functions are expressed as:

In saturated soil:

$$\varphi_{\mathrm{rp1}}^{\iota}\left(x,y\right) = A_{\mathrm{rp1}}^{\iota}\exp\left[\mathrm{i}k_{\mathrm{rp1}}\left(x\sin\theta_{\mathrm{rp1}}+y\cos\theta_{\mathrm{rp1}}\right)\right] \tag{16}$$

$$\varphi_{\mathrm{rp2}}^{\iota}\left(x,y\right) = A_{\mathrm{rp2}}^{\iota}\exp\left[\mathrm{i}k_{\mathrm{rp2}}\left(x\sin\theta_{\mathrm{rp2}}+y\cos\theta_{\mathrm{rp2}}\right)\right] \tag{17}$$

$$\boldsymbol{\psi}_{\mathrm{rs}}^{\iota}\left(x,y\right) = B_{\mathrm{rs}}^{\iota}\exp\left[\mathrm{i}k_{\mathrm{rs}}\left(x\sin\theta_{\mathrm{rs}} + y\cos\theta_{\mathrm{rs}}\right)\right] \tag{18}$$

Where k_{rp1}, k_{rp2} and k_{rs} represent the wavenumbers of reflected P_1, P_2 and S wave respectively; ϑ_{rp1}, ϑ_{rp2} and ϑ_{rs} represent the reflection angles. A_{rp1}^{ι}, A_{rp2}^{ι} and B_{rs}^{ι} represent the amplitude for the reflected waves in ι phase media and the relationship between the amplitude values is $\delta_{\mathrm{L1}} = A_{\mathrm{rp1}}^{\mathrm{f}}\big/A_{\mathrm{rp1}}^{\mathrm{s}}$, $\delta_{\mathrm{L2}} = A_{\mathrm{rp2}}^{\mathrm{f}}\big/A_{\mathrm{rp2}}^{\mathrm{s}}$ (Zhang et al., 2024).

In the water layer:

Transmission P wave:

$$\varphi_{\mathrm{t}}^{\mathrm{w}}\left(x,y\right) = A_{\mathrm{tp}}^{\mathrm{w}}\exp[\mathrm{i}k_{\mathrm{w}}(x_3\sin\theta_{\mathrm{w}} - y_3\cos\theta_{\mathrm{w}})] \tag{19}$$

Reflected P wave:

$$\varphi_{\mathrm{r}}^{\mathrm{w}}\left(x,y\right) = A_{\mathrm{rp}}^{\mathrm{w}}\exp[\mathrm{i}k_{\mathrm{w}}(x_3\sin\theta_{\mathrm{w}} + y_3\cos\theta_{\mathrm{w}})] \tag{20}$$

Where $A_{\mathrm{tp}}^{\mathrm{w}}$ and $A_{\mathrm{rp}}^{\mathrm{w}}$ are the amplitude coefficients of the transmitted and the reflected P waves, respectively, k_{w} is the wave number, θ_{w} is the reflection angle.

In cylindrical coordinates, it can be expressed as:

$$\boldsymbol{\psi}_{\mathrm{is}}^{\iota}\left(r_1,\theta_1\right) = B_{\mathrm{is}}^{\iota}\exp\left(\mathrm{i}dk_{\mathrm{is}}\cos\theta_{\mathrm{is}}\right)\exp\left[-\mathrm{i}k_{\mathrm{is}}r_1\cos\left(\theta_1 + \theta_{\mathrm{is}}\right)\right] \tag{21}$$

$$\varphi_{\mathrm{rp1}}^{\iota}(r_1,\theta_1) = A_{\mathrm{rp1}}^{\iota}\exp(-\mathrm{i}dk_{\mathrm{rp1}}\cos\theta_{\mathrm{rp1}})\exp[\mathrm{i}k_{\mathrm{rp1}}r_1\cos(\theta_1 - \theta_{\mathrm{rp1}})] \tag{22}$$

$$\varphi_{\mathrm{rp2}}^{\iota}(r_1,\theta_1) = A_{\mathrm{rp2}}^{\alpha}\exp(-\mathrm{i}dk_{\mathrm{rp2}}\cos\theta_{\mathrm{rp2}})\exp[\mathrm{i}k_{\mathrm{rp2}}r_1\cos(\theta_1-\theta_{\mathrm{rp2}})] \tag{23}$$

$$\psi_{\mathrm{rs}}^{\iota}\left(r_1,\theta_1\right) = B_{\mathrm{rs}}^{\iota}\exp\left(-\mathrm{i}dk_{\mathrm{rs}}\cos\theta_{\mathrm{rs}}\right)\exp\left[\mathrm{i}k_{\mathrm{rs}}r_1\cos\left(\theta_1-\theta_{\mathrm{rs}}\right)\right] \tag{24}$$

$$\varphi_{\mathrm{t}}^{\mathrm{w}}\left(x,y\right) = A_{\mathrm{tp}}^{\mathrm{w}}\exp\left[\mathrm{i}k_{\mathrm{w}}(d+h)\cos\theta_{\mathrm{w}}\right]\exp\left[-\mathrm{i}k_{\mathrm{w}}\cos\left(\theta_1+\theta_{\mathrm{w}}\right)\right] \tag{25}$$

$$\varphi_{\mathrm{r}}^{\mathrm{w}}\left(x,y\right) = A_{\mathrm{rp}}^{\mathrm{w}}\exp\left[\text{-}\mathrm{i}k_{\mathrm{w}}(d+h)\cos\theta_{\mathrm{w}}\right]\exp\left[\mathrm{i}k_{\mathrm{w}}\cos\left(\theta_1-\theta_{\mathrm{w}}\right)\right] \tag{26}$$

The above equation is expanded into Fourier-Bessel series form:

$$\psi_{\mathrm{is+rs}}^{\iota}\left(r_1,\theta_1\right) = \sum_{n=0}^{\infty} J_n\left(k_{\mathrm{is}}r_1\right)\left(C_{03,n}\sin n\theta_1 + D_{03,n}\cos n\theta_1\right) \tag{27}$$

$$\varphi_{\mathrm{rp1}}^{\iota}\left(r_1,\theta_1\right) = \sum_{n=0}^{\infty} J_n\left(k_{\mathrm{rp1}}r_1\right)\left(C_{01,n}\cos n\theta_1 + D_{01,n}\sin n\theta_1\right) \tag{28}$$

$$\varphi_{\mathrm{rp2}}^{\iota}(r_1,\theta_1) = \sum_{n=0}^{\infty} J_n(k_{rp2}r_1)(C_{02,n}\cos n\theta_1 + D_{02,n}\sin n\theta_1) \tag{29}$$

$$\varphi_{\mathrm{t+r}}^{\mathrm{w}}(r_1,\theta_1) = \sum_{n=0}^{\infty} J_n(k_{\mathrm{w}}r_1)(C_{04,n}\cos n\theta_1 + D_{04,n}\cos n\theta_1) \tag{30}$$

where:

$$C_{03,n} = \varepsilon_n \mathrm{i}^n \sin n\theta_{\mathrm{is}}\left[-B_{\mathrm{is}}^{\iota}\left(-1\right)^n\exp\left(\mathrm{i}dk_{\mathrm{is}}\cos\theta_{\mathrm{is}}\right) + B_{\mathrm{rs}}^{\iota}\exp\left(-\mathrm{i}dk_{\mathrm{is}}\cos\theta_{\mathrm{is}}\right)\right] \tag{31}$$

$$D_{03,n} = \varepsilon_n \mathrm{i}^n \cos n\theta_{\mathrm{is}}\left[B_{\mathrm{is}}^{\iota}\left(-1\right)^n\exp\left(\mathrm{i}dk_{\mathrm{is}}\cos\theta_{\mathrm{is}}\right) + B_{\mathrm{rs}}^{\iota}\exp\left(-\mathrm{i}dk_{\mathrm{is}}\cos\theta_{\mathrm{is}}\right)\right] \tag{32}$$

$$C_{01,n} = A_{\mathrm{rp1}}^{\iota}\varepsilon_n \mathrm{i}^n \cos n\theta_{\mathrm{rp1}}\exp\left(-\mathrm{i}dk_{\mathrm{rp1}}\cos\theta_{\mathrm{rp1}}\right) \tag{33}$$

$$D_{01,n} = A_{\mathrm{rp1}}^{\iota}\varepsilon_n \mathrm{i}^n \sin n\theta_{\mathrm{rp1}}\exp\left(-\mathrm{i}dk_{\mathrm{rp1}}\cos\theta_{\mathrm{rp1}}\right) \tag{34}$$

$$C_{02,n} = A_{\mathrm{rp2}}^{\iota}\varepsilon_n \mathrm{i}^n \cos n\theta_{\mathrm{rp2}}\exp\left(\text{-}\mathrm{i}dk_{\mathrm{rp2}}\cos\theta_{\mathrm{rp2}}\right) \tag{35}$$

$$D_{02,n} = A_{\mathrm{rp2}}^{\iota}\varepsilon_n \mathrm{i}^n \sin n\theta_{\mathrm{rp2}}\exp\left(\text{-}\mathrm{i}dk_{\mathrm{rp2}}\cos\theta_{\mathrm{rp2}}\right) \tag{36}$$

$$C_{04,n} = \varepsilon_n i^n \cos n\theta_{\mathrm{w}}\{[(-1)^n\exp[\mathrm{i}(d+h)k_{\mathrm{w}}\cos\theta_{\mathrm{w}}] + A_{\mathrm{r}}^{\mathrm{w}}\exp[-i(d+h)k_{\mathrm{w}}\cos\theta_{\mathrm{w}}]\} \tag{37}$$

$$D_{04,n} = \varepsilon_n i^n \sin n\theta_{\mathrm{w}}\{-(-1)^n\exp[\mathrm{i}(d+h)k_{\mathrm{w}}\cos\theta_{\mathrm{w}}] + A_{\mathrm{r}}^{\mathrm{w}}\exp[-i(d+h)k_{\mathrm{w}}\cos\theta_{\mathrm{w}}]\} \tag{38}$$

where: ε_n=2 when n=0, ε_n = 2 when n≥1.

In the saturated soil layer, scattered P_1, P_2, and SV waves are generated by both the circular tunnel and the large circular arc approximation. The scattered wave fields in the saturated soil and water layers are represented by Fourier-Bessel series. In the r_1-ϑ_1 coordinate system, the scattered wave field from the circular arc boundary satisfies the Sommerfeld condition at infinity, allowing the Fourier-Bessel series to be expressed as:

In saturated soil:

$$\varphi_{\mathrm{dp1}}^{\iota}\left(r_1,\theta_1\right)=\sum_{n=0}^{\infty}H_n^{(1)}\left(k_{\mathrm{rp1}}r_1\right)\left(C_{11,n}^{(1)}\cos n\theta_1+D_{11,n}^{(1)}\sin n\theta_1\right) \tag{39}$$

$$\varphi_{\mathrm{dp2}}^{\iota}\left(r_1,\theta_1\right)=\sum_{n=0}^{\infty}H_n^{(1)}\left(k_{\mathrm{rp2}}r_1\right)\left(C_{12,n}^{(1)}\cos n\theta_1+D_{12,n}^{(1)}\sin n\theta_1\right) \tag{40}$$

$$\psi_{\mathrm{ds}}^{\iota}\left(r_1,\theta_1\right)=\sum_{n=0}^{\infty}H_n^{(1)}\left(k_{\mathrm{rs1}}r_1\right)\left(C_{14,n}^{(1)}\sin n\theta_1+D_{14,n}^{(1)}\cos n\theta_1\right) \tag{41}$$

where $J_m(\ \ )$ and $H_n^{(1)}(\ \ )$ are Bessel functions and Hankel functions, respectively.

As all wave potential functions are in the (r_1, ϑ_1) coordinate system, satisfying the boundary condition at y=0 is challenging. This study adopts the method from references (Cao and Lee, 1979, Lee and Cao, 1989), using a circular arc with radius R and center at O_2 (Figure 1) to simulate the water-soil interface and the free surface of the water layer. Therefore, the results represent an approximate analytical solution. Studies (Ma et al., 2023; Liang et al., 2001; Shi et al., 2024; Zhao and Ma, 2024) indicate that when the radius of the large circular arc R is sufficiently large ($R >> a$), such as $R > 50a$, the computational error from this approximation is minimal, yielding satisfactory results.

In the r_2-ϑ_2 coordinate system, the scattering wave field is generated due to the existence of the large arc boundary, which is expressed as follows:

In saturated soil:

$$\varphi_{\mathrm{ap1}}^{\iota}\left(r_2,\theta_2\right)=\sum_{m=0}^{\infty}J_m\left(k_{\mathrm{rp1}}r_2\right)\left(C_{21,m}^{(2)}\cos m\theta_2+D_{21,m}^{(2)}\sin m\theta_2\right) \tag{42}$$

$$\varphi_{\mathrm{ap2}}^{\iota}\left(r_2,\theta_2\right)=\sum_{m=0}^{\infty}J_m\left(k_{\mathrm{rp2}}r_2\right)\left(C_{22,m}^{(2)}\cos m\theta_2+D_{22,m}^{(2)}\sin m\theta_2\right) \tag{43}$$

$$\psi_{\mathrm{as}}^{\iota}\left(r_2,\theta_2\right)=\sum_{m=0}^{\infty}J_m\left(k_{\mathrm{rs1}}r_2\right)\left(C_{24,m}^{(2)}\sin m\theta_2+D_{24,m}^{(2)}\cos m\theta_2\right) \tag{44}$$

In the water layer:

$$\varphi_{\mathrm{a1}}^{\mathrm{w}}(r_2,\theta_2)=\sum_{m=0}^{\infty}J_m(k_{\mathrm{w}}r_2)(C_{31,m}^{(2)}\cos m\theta_2+D_{31,m}^{(2)}\sin m\theta_2) \tag{45}$$

$$\varphi_{\mathrm{a2}}^{\mathrm{w}}(r_2,\theta_2)=\sum_{m=0}^{\infty}H_m(k_{\mathrm{w}}r_2)(C_{32,n}^{(2)}\cos m\theta_2+D_{32,n}^{(2)}\sin m\theta_2) \tag{46}$$

The total wave potential function is:

In saturated soil:

$$\varphi^{\iota} = \varphi^{\iota}_{\mathrm{rp1}} + \varphi^{\iota}_{\mathrm{rp2}} + \varphi^{\iota}_{\mathrm{dp1}} + \varphi^{\iota}_{\mathrm{dp2}} + \varphi^{\iota}_{\mathrm{ap1}} + \varphi^{\iota}_{\mathrm{ap2}} \tag{47}$$

$$\psi^{\iota} = \psi^{\iota}_{\mathrm{is}} + \psi^{\iota}_{rs} + \psi^{\iota}_{ds} + \psi^{\iota}_{as} \tag{48}$$

In the water layer:

$$\varphi^{\mathrm{W}} = \varphi^{\mathrm{W}}_{\mathrm{t}} + \varphi^{\mathrm{W}}_{\mathrm{r}} + \varphi^{\mathrm{W}}_{\mathrm{a1}} + \varphi^{\mathrm{W}}_{\mathrm{a2}} \tag{49}$$

According to the Graf addition formula, the above wave function is transformed into coordinates:

$$\varphi^{\mathrm{W}} = \varphi^{\mathrm{W}}_{\mathrm{t}} + \varphi^{\mathrm{W}}_{\mathrm{r}} + \varphi^{\mathrm{W}}_{\mathrm{a1}} + \varphi^{\mathrm{W}}_{\mathrm{a2}} \tag{50}$$

where D is the distance from O_1 point to O_2 point, $C_n()$ can be $J_n()$ function or $H_n^{(1)}()$ function.

Therefore, the coordinate transformation of Eq. (39) - (46) can be obtained:

$$\varphi^{\iota}_{\mathrm{dp1}}(r_2,\theta_2) = \sum_{m=0}^{\infty} J_m(k_{rp1}r_2)(C^{(2)}_{11,n}\cos m\theta_2 + D^{(2)}_{11,n}\sin m\theta_2) \tag{51}$$

$$\varphi^{\iota}_{\mathrm{dp2}}(r_2,\theta_2) = \sum_{m=0}^{\infty} J_m(k_{\mathrm{rp2}}r_2)(C^{(2)}_{12,n}\cos m\theta_2 + D^{(2)}_{12,n}\sin m\theta_2) \tag{52}$$

$$\psi^{\iota}_{ds}(r_2,\theta_2) = \sum_{m=0}^{\infty} J_m(k_{rs}r_2)(C^{(2)}_{13,n}\sin m\theta_2 + D^{(2)}_{13,n}\cos m\theta_2) \tag{53}$$

$$\varphi^{\iota}_{\mathrm{ap1}}(r_1,\theta_1) = \sum_{n=0}^{\infty} J_n(k_{rp1}r_1)(C^{(1)}_{21,n}\cos n\theta_1 + D^{(1)}_{21,n}\sin n\theta_1) \tag{54}$$

$$\varphi^{\iota}_{\mathrm{ap2}}(r_1,\theta_1) = \sum_{n=0}^{\infty} J_n(k_{rp2}r_1)(C^{(1)}_{22,n}\cos n\theta_1 + D^{(1)}_{22,n}\sin n\theta_1) \tag{55}$$

$$\psi^{\iota}_{\mathrm{as}}(r_1,\theta_1) = \sum_{n=0}^{\infty} J_n(k_{rs}r_1)(C^{(1)}_{23,n}\sin n\theta_1 + D^{(1)}_{23,n}\cos n\theta_1) \tag{56}$$

$$\varphi^{\mathrm{w}}_{\mathrm{a1}}(r_1,\theta_1) = \sum_{n=0}^{\infty} J_n(k_{\mathrm{w}}r_1)(C^{(1)}_{31,n}\cos n\theta_1 + D^{(1)}_{31,n}\sin n\theta_1) \tag{57}$$

$$\varphi^{\mathrm{w}}_{\mathrm{a2}}(r_1,\theta_1) = \sum_{m=0}^{\infty} J_m(k_{\mathrm{w}}r_1)(C^{(1)}_{32,m}\cos m\theta_1 + D^{(1)}_{32,m}\sin m\theta_1) \tag{58}$$

where:

$$\begin{bmatrix} C_{11,m}^{(2)} \\ C_{12,m}^{(2)} \\ D_{14,m}^{(2)} \end{bmatrix} = \sum_{n=0}^{\infty} \begin{bmatrix} F2_{nm}^{+}(k_{rp1}D) & & \\ & F2_{nm}^{+}(k_{rp2}D) & \\ & & F2_{nm}^{+}(k_{rs}D) \end{bmatrix} \begin{bmatrix} C_{11,n}^{(1)} \\ C_{12,n}^{(1)} \\ D_{14,n}^{(1)} \end{bmatrix} \tag{59}$$

$$\begin{bmatrix} D_{11,m}^{(2)} \\ D_{12,m}^{(2)} \\ C_{14,m}^{(2)} \end{bmatrix} = \sum_{n=0}^{\infty} \begin{bmatrix} F2_{nm}^{-}(k_{rp1}D) & & \\ & F2_{nm}^{-}(k_{rp2}D) & \\ & & F2_{nm}^{-}(k_{rs}D) \end{bmatrix} \begin{bmatrix} D_{11,n}^{(1)} \\ D_{12,n}^{(1)} \\ C_{14,n}^{(1)} \end{bmatrix} \tag{60}$$

$$\begin{bmatrix} C_{21,n}^{(1)} \\ C_{22,n}^{(1)} \\ C_{31,n}^{(1)} \\ C_{32,n}^{(1)} \\ D_{23,n}^{(1)} \end{bmatrix} = \sum_{n=0}^{\infty} \begin{bmatrix} F1_{nm}^{+}(k_{\mathrm{rp1}}D) & & & & \\ & F1_{nm}^{+}(k_{\mathrm{rp2}}D) & & & \\ & & F1_{nm}^{+}(k_{\mathrm{w}}D) & & \\ & & & F1_{nm}^{+}(k_{\mathrm{w}}D) & \\ & & & & F1_{nm}^{+}(k_{\mathrm{rs}}D) \end{bmatrix} \begin{bmatrix} C_{21,m}^{(2)} \\ C_{22,m}^{(2)} \\ C_{31,m}^{(1)} \\ C_{32,m}^{(1)} \\ D_{23,m}^{(2)} \end{bmatrix} \tag{61}$$

$$\begin{bmatrix} D_{21,n}^{(1)} \\ D_{22,n}^{(1)} \\ D_{31,n}^{(1)} \\ D_{32,n}^{(1)} \\ C_{23,n}^{(1)} \end{bmatrix} = \sum_{n=0}^{\infty} \begin{bmatrix} F1_{nm}^{-}(k_{\mathrm{rp1}}D) & & & & \\ & F1_{nm}^{-}(k_{\mathrm{rp2}}D) & & & \\ & & F1_{nm}^{-}(k_{\mathrm{w}}D) & & \\ & & & F1_{nm}^{-}(k_{\mathrm{w}}D) & \\ & & & & F1_{nm}^{-}(k_{\mathrm{rs}}D) \end{bmatrix} \begin{bmatrix} D_{21,m}^{(2)} \\ D_{22,m}^{(2)} \\ D_{31,m}^{(1)} \\ D_{32,m}^{(1)} \\ C_{23,m}^{(2)} \end{bmatrix} \tag{62}$$

where:

$$F1_{nm}^{\pm}(kD) = \frac{1}{2}\varepsilon_n[J_{n+m}(kD) \pm (-1)^m J_{n-m}(kD)] \tag{63}$$

$$F2_{nm}^{\pm}(kD) = \frac{1}{2}\varepsilon_m[H_{m+n}(kD) \pm (-1)^n H_{m-n}(kD)] \tag{64}$$

This research assumes that the surface and the tunnel surface are permeable boundaries, and the boundary conditions are as follows:

On the surface of the water $r_2=R+h$:

$$\sigma_{yy}^{\mathrm{w}} = 0 \tag{65}$$

On the tunnel surface $r_1 = a$:

$$\sigma_{rr}^{\mathrm{S}} = 0, \sigma_{r\theta}^{\mathrm{S}} = 0, \sigma_{rr}^{\mathrm{L}} = 0 \tag{66}$$

At the soil-water interface $r_2 = R_1$:

$$\left.\begin{array}{l}\left(1-n\right)u_r^{\mathrm{S}}+nu_r^{\mathrm{L}}=u_r^{\mathrm{w}}\\ \sigma_{rr}^{\mathrm{S}}+\sigma_{rr}^{\mathrm{L}}=-\sigma_{rr}^{\mathrm{w}}\\ \sigma_{rr}^{\mathrm{L}}=-n\sigma_{rr}^{\mathrm{w}}\\ \sigma_{r\theta}^{\mathrm{S}}=0\end{array}\right\} \tag{67}$$

The stress can be written as the following form:
In the water layer:

$$\left.\begin{array}{l}\sigma_{yy}^{w}=-K_{\mathrm{W}}(\dfrac{\partial^2\varphi^{\mathrm{w}}}{\partial x^2}+\dfrac{\partial^2\varphi^{\mathrm{w}}}{\partial y^2})\\ u_y^{\mathrm{w}}=\dfrac{\partial\varphi^{\mathrm{w}}}{\partial y}\end{array}\right\} \tag{68}$$

In saturated soil:

$$\left.\begin{array}{l}\sigma_{yy}^{\mathrm{S}}=(\lambda+\alpha^2M)\nabla^2\varphi^{\mathrm{s}}+\alpha M\nabla^2\varphi^{\mathrm{f}}+2\mu\ (\dfrac{\partial^2\varphi^{\mathrm{s}}}{\partial y^2}+\dfrac{\partial^2\psi^{\mathrm{s}}}{\partial x\partial y})\\ \sigma_{xy}^{\mathrm{S}}=2\mu\dfrac{\partial^2\varphi^{\mathrm{s}}}{\partial x\partial y}+\mu(\dfrac{\partial^2\psi^{\mathrm{s}}}{\partial x^2}-\dfrac{\partial^2\psi^{\mathrm{s}}}{\partial y^2})\\ \sigma_{yy}^{\mathrm{f}}=-M(\nabla^2\varphi_{\mathrm{f}}+\alpha\nabla^2\varphi_{\mathrm{s}}),\ u_y^{\mathrm{S}}=\dfrac{\partial\varphi^{\mathrm{S}}}{\partial y}+\dfrac{\partial\psi^{\mathrm{S}}}{\partial x}\\ u_x^{\mathrm{S}}=\dfrac{\partial\varphi^{\mathrm{S}}}{\partial x}-\dfrac{\partial\psi^{\mathrm{S}}}{\partial y},\ u_y^{\mathrm{f}}=\dfrac{\partial\varphi^{\mathrm{f}}}{\partial z}+\dfrac{\partial\psi^{\mathrm{f}}}{\partial x}\end{array}\right\} \tag{69}$$

The expression in the cylindrical coordinate system is:
In the water layer:

$$\sigma_{rr}^{w}=-K_{\mathrm{W}}(\frac{\partial^2\varphi^{\mathrm{w}}}{\partial r^2}+\frac{1}{r}\frac{\partial\varphi^{\mathrm{w}}}{\partial r}+\frac{1}{r^2}\frac{\partial^2\varphi^{\mathrm{w}}}{\partial\theta^2}) \tag{70}$$

$$u_r^{\mathrm{w}}=\frac{\partial\varphi^{\mathrm{w}}}{\partial r} \tag{71}$$

In saturated soil:

$$\begin{array}{l}\sigma_{rr}^{\mathrm{S}}=(\lambda+\alpha^2M)\left(\dfrac{\partial^2\varphi^{\mathrm{S}}}{\partial r^2}+\dfrac{1}{r}\dfrac{\partial\varphi^{\mathrm{S}}}{\partial r}+\dfrac{1}{r^2}\dfrac{\partial^2\varphi^{\mathrm{S}}}{\partial\theta^2}\right)+\alpha M\\ \left(\dfrac{\partial^2\varphi^{\mathrm{f}}}{\partial r^2}+\dfrac{1}{r}\dfrac{\partial\varphi^{\mathrm{f}}}{\partial r}+\dfrac{1}{r^2}\dfrac{\partial^2\varphi^{\mathrm{f}}}{\partial\theta^2}\right)+2\mu\left(\dfrac{\partial^2\varphi^{\mathrm{S}}}{\partial r^2}+\dfrac{1}{r}\dfrac{\partial^2\psi^{\mathrm{S}}}{\partial r\partial\theta}-\dfrac{1}{r^2}\dfrac{\partial\psi^{\mathrm{S}}}{\partial\theta}\right)\end{array} \tag{72}$$

$$\sigma_{r\theta}^{\mathrm{S}}=\mu\left[2\left(\frac{1}{r}\frac{\partial^2\varphi^{S}}{\partial r\partial\theta}-\frac{1}{r^2}\frac{\partial\varphi^{S}}{\partial\theta}\right)+\frac{1}{r^2}\frac{\partial^2\psi^{S}}{\partial\theta^2}+\frac{1}{r}\frac{\partial\psi^{S}}{\partial r}-\frac{\partial^2\psi^{S}}{\partial r^2}\right] \tag{73}$$

$$\sigma_{rr}^{\mathrm{f}}=-M(\frac{\partial^2\varphi^{\mathrm{f}}}{\partial r^2}+\frac{1}{r}\frac{\partial\varphi^{\mathrm{f}}}{\partial r}+\frac{1}{r^2}\frac{\partial^2\varphi^{\mathrm{f}}}{\partial\theta^2})-M\alpha\left(\frac{\partial^2\varphi^{\mathrm{S}}}{\partial r^2}+\frac{1}{r}\frac{\partial\varphi^{\mathrm{S}}}{\partial r}+\frac{1}{r^2}\frac{\partial^2\varphi^{\mathrm{S}}}{\partial\theta^2}\right) \tag{74}$$

$$u_r^{\mathrm{S}} = \frac{\partial \varphi^{\mathrm{S}}}{\partial r} + \frac{1}{r}\frac{\partial \psi^{\mathrm{S}}}{\partial \theta}, u_\theta^{\mathrm{S}} = \frac{1}{r}\frac{\partial \varphi^{\mathrm{S}}}{\partial \theta} - \frac{\partial \psi^{\mathrm{S}}}{\partial r} \tag{75}$$

$$u_r^{\mathrm{f}} = \frac{\partial \varphi^{\mathrm{f}}}{\partial r} + \frac{1}{r}\frac{\partial \psi^{\mathrm{f}}}{\partial \theta}, u_\theta^{\mathrm{f}} = \frac{1}{r}\frac{\partial \varphi^{\mathrm{f}}}{\partial \theta} - \frac{\partial \psi^{\mathrm{f}}}{\partial r} \tag{76}$$

where: The subscripts rr and r represent the radial direction, and rθ and θ represent the tangential direction.

Bringing Eq. (57) and Eq. (58) into boundary condition (65):

$$\begin{aligned}&\sum_{m=0}^{\infty} V_{31}^{s(1)}\left(m, R+hw\right)(C_{31,m}^{(2)})\cos m\theta_2 + \sum_{m=0}^{\infty} V_{31}^{s(1)}\left(m, R+hw\right)(D_{31,m}^{(2)})\sin m\theta_2 \\ &+\sum_{m=0}^{\infty} V_{31}^{s(2)}\left(m, R+hw\right)(C_{32,m}^{(2)})\cos m\theta_2 + \sum_{m=0}^{\infty} V_{31}^{s(2)}\left(m, R+hw\right)(D_{32,m}^{(2)})\sin m\theta_2 = 0\end{aligned} \tag{77}$$

In order to satisfy the above equation, Equation (77) must satisfy:

$$\begin{cases} -\dfrac{V_{31}^{s(1)}\left(m, R+hw\right)C_{31,m}^{(2)}}{V_{31}^{s(2)}\left(m, R+hw\right)} = C_{32,m}^{(2)} \\ -\dfrac{V_{31}^{s(1)}\left(m, R+hw\right)D_{31,m}^{(2)}}{V_{31}^{s(2)}\left(m, R+hw\right)} = D_{32,m}^{(2)} \end{cases} \tag{78}$$

Bringing Eq. (39)-(41) and Eq. (54)-(56) into boundary condition (66):

$$\begin{aligned}&\sum_{n=0}^{\infty}\begin{bmatrix} E_{111}^{s(3)}\left(n,b\right) & E_{112}^{s(3)}\left(n,b\right) & E_{114}^{s(3)+}\left(n,b\right) \\ E_{211}^{s(3)-}\left(n,b\right) & E_{212}^{s(3)-}\left(n,b\right) & E_{214}^{s(3)}\left(n,b\right) \\ E_{311}^{s(3)}\left(n,b\right) & E_{312}^{s(3)}\left(n,b\right) & 0 \end{bmatrix}\begin{Bmatrix} C_{11,n}^{(1)} \\ C_{12,n}^{(1)} \\ C_{13,n}^{(1)} \end{Bmatrix}\begin{Bmatrix} \cos n\theta_1 \\ \sin n\theta_1 \\ \cos n\theta_1 \\ \cos n\theta_1 \end{Bmatrix} + \\ &\sum_{n=0}^{\infty}\begin{bmatrix} E_{111}^{s(1)}\left(n,b\right) & E_{112}^{s(1)}\left(n,b\right) & E_{114}^{s(1)+}\left(n,b\right) \\ E_{211}^{s(1)-}\left(n,b\right) & E_{212}^{s(1)-}\left(n,b\right) & E_{214}^{s(1)}\left(n,b\right) \\ E_{311}^{s(1)}\left(n,b\right) & E_{312}^{s(1)}\left(n,b\right) & 0 \end{bmatrix}\begin{Bmatrix} C_{21,n}^{(1)} + C_{01,n} \\ C_{22,n}^{(1)} + C_{02,n} \\ C_{23,n}^{(1)} + C_{03,n} \end{Bmatrix}\begin{Bmatrix} \cos n\theta_1 \\ \sin n\theta_1 \\ \cos n\theta_1 \\ \cos n\theta_1 \end{Bmatrix} + \\ &\sum_{n=0}^{\infty}\begin{bmatrix} E_{111}^{s(3)}\left(n,b\right) & E_{112}^{s(3)}\left(n,b\right) & E_{114}^{s(3)-}\left(n,b\right) \\ E_{211}^{s(3)+}\left(n,b\right) & E_{212}^{s(3)+}\left(n,b\right) & E_{214}^{s(3)}\left(n,b\right) \\ E_{311}^{s(3)}\left(n,b\right) & E_{312}^{s(3)}\left(n,b\right) & 0 \end{bmatrix}\begin{Bmatrix} D_{11,n}^{(1)} \\ D_{12,n}^{(1)} \\ D_{13,n}^{(1)} \end{Bmatrix}\begin{Bmatrix} \sin n\theta_1 \\ \cos n\theta_1 \\ \sin n\theta_1 \\ \sin n\theta_1 \end{Bmatrix} + \\ &\sum_{n=0}^{\infty}\begin{bmatrix} E_{111}^{s(1)}\left(n,b\right) & E_{112}^{s(1)}\left(n,b\right) & E_{114}^{s(1)-}\left(n,b\right) \\ E_{211}^{s(1)+}\left(n,b\right) & E_{212}^{s(1)+}\left(n,b\right) & E_{214}^{s(1)}\left(n,b\right) \\ E_{311}^{s(1)}\left(n,b\right) & E_{312}^{s(1)}\left(n,b\right) & 0 \end{bmatrix}\begin{Bmatrix} D_{21,n}^{(1)} + D_{01,n} \\ D_{22,n}^{(1)} + D_{02,n} \\ D_{23,n}^{(1)} + D_{03,n} \end{Bmatrix}\begin{Bmatrix} \sin n\theta_1 \\ \cos n\theta_1 \\ \sin n\theta_1 \\ \sin n\theta_1 \end{Bmatrix} = \begin{Bmatrix} 0 \\ 0 \\ 0 \\ 0 \end{Bmatrix}\end{aligned} \tag{79}$$

Bringing Eq. (42)-(44) and Eq. (51)-(53) into boundary condition (67):

$$\sum_{m=0}^{\infty}\begin{bmatrix} V_{111}^{s(1)}(m,R) \\ V_{211}^{s(1)}(m,R) \\ V_{311}^{s(1)}(m,R) \\ 0 \end{bmatrix}(C_{31,m}^{(2)})\begin{Bmatrix} \cos m\theta_2 \\ \cos m\theta_2 \\ \cos m\theta_2 \\ \sin m\theta_2 \end{Bmatrix}+\sum_{m=0}^{\infty}\begin{bmatrix} V_{111}^{s(1)}(m,R) \\ V_{211}^{s(1)}(m,R) \\ V_{311}^{s(1)}(m,R) \\ 0 \end{bmatrix}(D_{31,m}^{(2)})\begin{Bmatrix} \sin m\theta_2 \\ \sin m\theta_2 \\ \sin m\theta_2 \\ \cos m\theta_2 \end{Bmatrix}$$
$$+\sum_{m=0}^{\infty}\begin{bmatrix} V_{111}^{s(2)}(m,R) \\ V_{211}^{s(2)}(m,R) \\ V_{311}^{s(2)}(m,R) \\ 0 \end{bmatrix}(C_{32,m}^{(2)})\begin{Bmatrix} \cos m\theta_2 \\ \cos m\theta_2 \\ \cos m\theta_2 \\ \sin m\theta_2 \end{Bmatrix}+\sum_{m=0}^{\infty}\begin{bmatrix} V_{111}^{s(2)}(m,R) \\ V_{211}^{s(2)}(m,R) \\ V_{311}^{s(2)}(m,R) \\ 0 \end{bmatrix}(D_{32,m}^{(2)})\begin{Bmatrix} \sin m\theta_2 \\ \sin m\theta_2 \\ \sin m\theta_2 \\ \cos m\theta_2 \end{Bmatrix}=$$
$$\sum_{m=0}^{\infty}\begin{bmatrix} E_{111}^{s(1)}(m,R) & E_{112}^{s(1)}(m,R) & E_{113}^{s(1)+}(m,R) \\ E_{211}^{s(1)}(m,R) & E_{212}^{s(1)}(m,R) & E_{213}^{s(1)+}(m,R) \\ E_{311}^{s(1)}(m,R) & E_{312}^{s(1)}(m,R) & 0 \\ E_{411}^{s(1)+}(m,R) & E_{412}^{s(1)+}(m,R) & E_{413}^{s(1)}(m,R) \end{bmatrix}\begin{Bmatrix} C_{11,m}^{(2)}+C_{21,m}^{(2)} \\ C_{12,m}^{(2)}+C_{22,m}^{(2)} \\ C_{13,m}^{(2)}+C_{23,m}^{(2)} \end{Bmatrix}\begin{Bmatrix} \cos m\theta_2 \\ \cos m\theta_2 \\ \cos m\theta_2 \\ \sin m\theta_2 \end{Bmatrix}+$$
$$\sum_{m=0}^{\infty}\begin{bmatrix} E_{111}^{s(1)}(m,R) & E_{112}^{s(1)}(m,R) & E_{113}^{s(1)-}(m,R) \\ E_{211}^{s(1)}(m,R) & E_{212}^{s(1)}(m,R) & E_{213}^{s(1)-}(m,R) \\ E_{311}^{s(1)}(m,R) & E_{312}^{s(1)}(m,R) & 0 \\ E_{411}^{s(1)-}(m,R) & E_{412}^{s(1)-}(m,R) & E_{413}^{s(1)}(m,R) \end{bmatrix}\begin{Bmatrix} D_{11,m}^{(2)}+D_{21,m}^{(2)} \\ D_{12,m}^{(2)}+D_{22,m}^{(2)} \\ D_{13,m}^{(2)}+D_{23,m}^{(2)} \end{Bmatrix}\begin{Bmatrix} \sin m\theta_2 \\ \sin m\theta_2 \\ \sin m\theta_2 \\ \cos m\theta_2 \end{Bmatrix} \tag{80}$$

where:

$$E_{11j}^{s(1)}(m,R)=-\left(2C_{n-1}^{(i)}(k_{\mathrm{rp}j}r)k_{\mathrm{rp}j}\mu r+C_n^{(i)}(k_{\mathrm{rp}j}r)\left(k_{\mathrm{rp}j}^2\left(M\alpha^2+M\alpha\delta_{\mathrm{L}j}+\lambda+2\mu\right)r^2-2\mu\left(m^2+m\right)\right)\right)$$

$$E_{11k}^{s(1)\mp}(m,R)=\mp 2m\mu\left(-C_{n-1}^{(i)}(k_{\mathrm{rs}}r)k_{\mathrm{rs}}r+mC_n^{(i)}(k_{\mathrm{rs}}r)+C_n^{(i)}(k_{\mathrm{rs}}r)\right)$$

$$E_{21k}^{s(1)}(m,R)=-2\left(-C_{n-1}^{(i)}(k_{\mathrm{rs}}r)k_{\mathrm{rs}}r+C_n^{(i)}(k_{\mathrm{rs}}r)\left(n-\frac{1}{2}{k_{\mathrm{rs}}}^2r^2+m^2\right)\right)\mu$$

$$E_{21j}^{s(1)\mp}(m,R)=\pm 2m\left(-C_{n-1}^{(i)}(k_{\mathrm{rp}j}r)k_{\mathrm{rp}j}r+(m+1)C_n^{(i)}(k_{\mathrm{rp}j}r)\right)\mu$$

$$E_{31j}^{s(1)}(m,R)=M{k_{\mathrm{rp}j}}^2(\alpha+\delta_{\mathrm{L}j})C_n^{(i)}(k_{\mathrm{rp}j}r)$$

3 Verification

Introducing a dimensionless frequency:

$$\eta=2a/\lambda_\beta \tag{81}$$

Based on the Cauchy (Zhong and Zhang., 2010; Yang., 2009) criterion, the convergence of the displacement error is determined:

$$e(n;\,r_1,\,\theta_1)=|\,u(n+1;\,r_1,\,\theta_1)-u(n;\,r_1,\,\theta_1)\,| \tag{82}$$

As shown in Figure 2, at the midpoint on the tunnel surface (x=0, y=h), the relationship between computational error and truncation terms demonstrates the reasonableness of the chosen truncation terms.

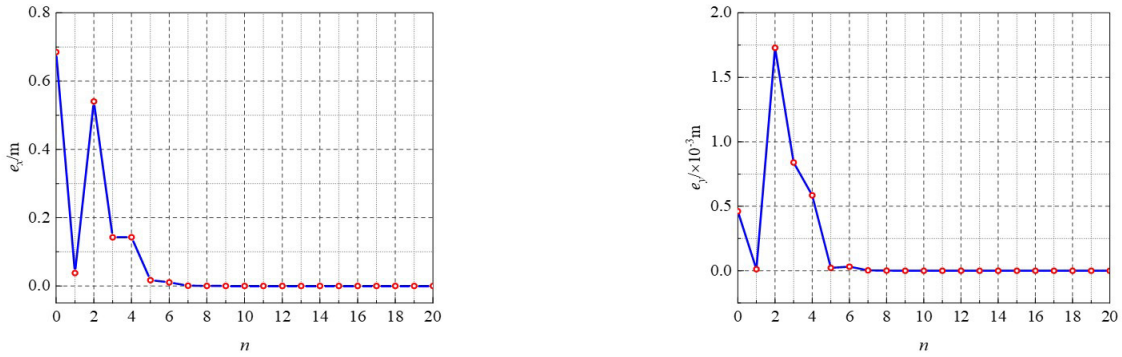

(a) e_x (b) e_y

Figure 2 The curve of error

Based on Zhong and Zhang (2010) the large circular arc radius R is set to 10^7a, which ensures the accuracy of numerical calculations. To verify the accuracy, the underwater tunnel is simplified to a circular tunnel in a saturated half-space. Detailed parameters are provided in reference (Liang and Liu, 2009). As shown in Figure 3, compared to the solution derived by Liang and Liu (2009) using the indirect boundary integral equation method, the displacement distribution curves are generally similar, with only minor local deviations. At the tunnel center (x=0, y=d), the horizontal displacement differs by 0.7%, while the vertical displacement shows a 10.6% difference. On both tunnel sides (x=±a, y=0), the horizontal displacement varies by 4.7% and the vertical displacement by 7.3%. These minor differences are primarily due to the distinct methods used in this study and the literature, but both solutions exhibit the same trend, validating the method's correctness.

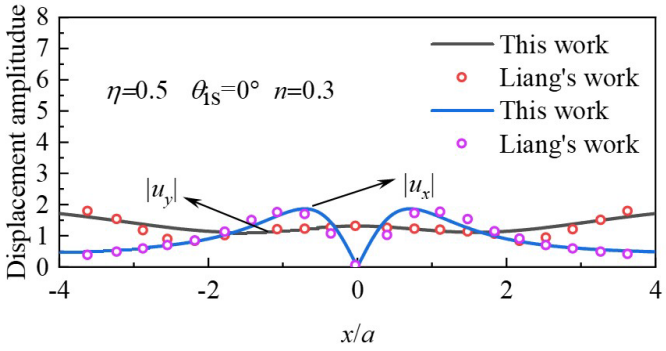

Figure 3 The curve of comparative verification.

4 Example analysis

This section analyzes the effects of SV wave incidence, incident angle, frequency, tunnel burial depth, and soil porosity on horizontal displacement, vertical displacement at the water-soil interface, and DSCF on the tunnel surface. For the computational analysis, the water layer's bulk modulus K_w is 2000 MPa, and its density ρ_w is 1000 kg/m^3. Physical and mechanical parameters for the saturated soil site are adopted from reference (Liu., 2015), as shown in Table 1.

Table 1. Physical and mechanical parameters

Material parameters	Porosity	Density of soil particle	Density of liquid	Viscosity coefficient of solid	Bulk modulus of soil particles	Bulk modulus of liquid	Solid Skeleton Bulk Modulus
Symbol (unit)	n	ρ_s (Kg/m^3)	ρ_f (Kg/m^3)	η_b (Pa•s)	K_s (GPa)	K_f (GPa)	K (MPa)
Magnitude	0.3	2650	1000	1×10^{-3}	36	2	24
Material parameters	Permeability coefficient	Lamé constant	Lamé constant				
Symbol (unit)	k_b (m/s)	μ (GPa)	λ (GPa)				
Magnitude	1×10^{-12}	18	12				

4.1 *Influence of incidence angle*

Figures 4 and 5 illustrate the impact of incident angle (ϑ_{is} = 0°, 15°, 30°) and frequency (η = 0.5, 1, 2) on the displacement at the water-soil interface and the Dynamic Stress Concentration Factor (DSCF) around the tunnel. As shown in figure 4, at a low frequency (η = 0.5), the maximum horizontal displacement occurs at ϑ_{is} = 0°, suggesting that for nearly vertical wave incidence, the horizontal response dominate. In contrast, vertical displacement reaches its peak at ϑ_{is} = 30°, indicating that as the angle of incidence increases, vertical forces become more significant. This finding implies that tunnels subjected to seismic waves from larger angles might experience greater vertical stress, which is critical for structural design in seismic regions. As the frequency increases to η = 1.0, the trend remains consistent, with horizontal displacement decreasing and vertical displacement increasing as the incident angle grows. This suggests that higher frequencies combined with steep angles of incidence amplify vertical stresses, potentially leading to greater deformation along the tunnel walls, requiring reinforcement in tunnel design for high-frequency seismic events. At η = 2.0, horizontal displacement near the tunnel top ($-1 \le x/a \le 1$) is smaller than on the sides, showing that at higher frequencies, wave interaction becomes more localized around the tunnel sides. In terms of stress concentration, Figure 5 highlights that DSCF reaches its peak at ϑ_{is} = 30°, with its maximum value growing with increasing incidence angle. This suggests that, for underwater tunnels, obliquely incident seismic waves impose the highest stresses, especially at moderate to high frequencies. In practical terms, tunnel designs in regions prone to oblique seismic waves should prioritize stress management and include reinforcement strategies at critical points along the tunnel structure.

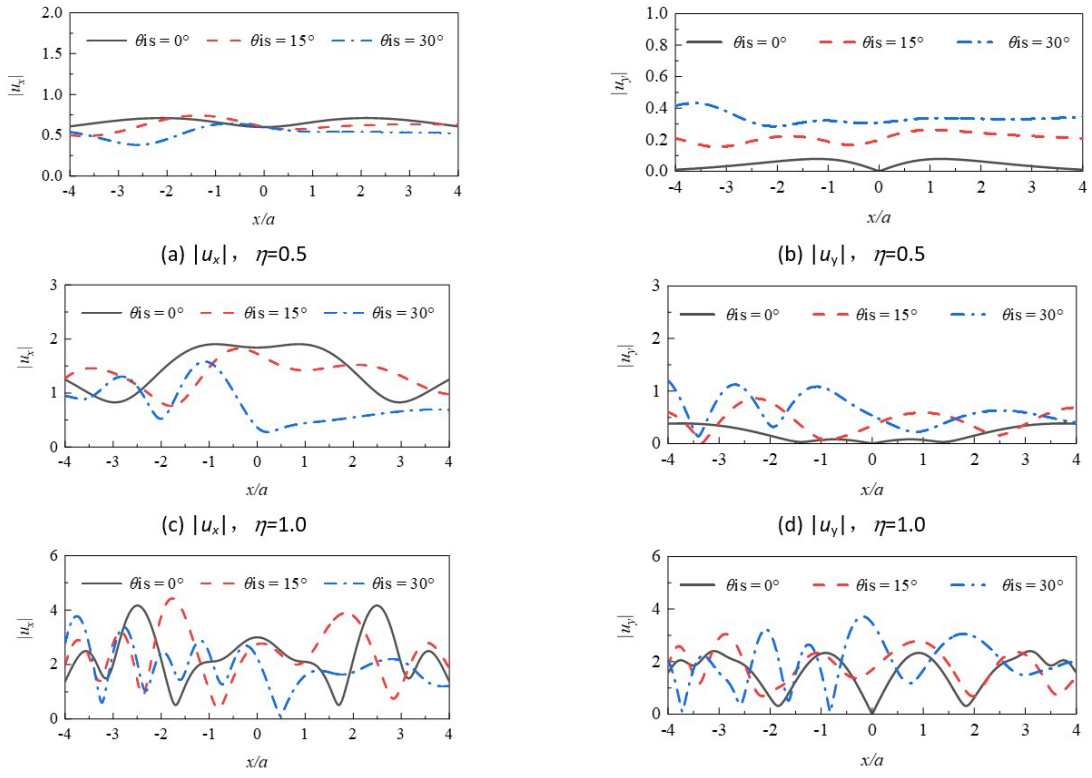

(a) $|u_x|$, η=0.5 (b) $|u_y|$, η=0.5

(c) $|u_x|$, η=1.0 (d) $|u_y|$, η=1.0

(e) $|u_x|$, η=2.0 (f) $|u_y|$, η=2.0

Figure 4 Effect of incident angle on the displacement

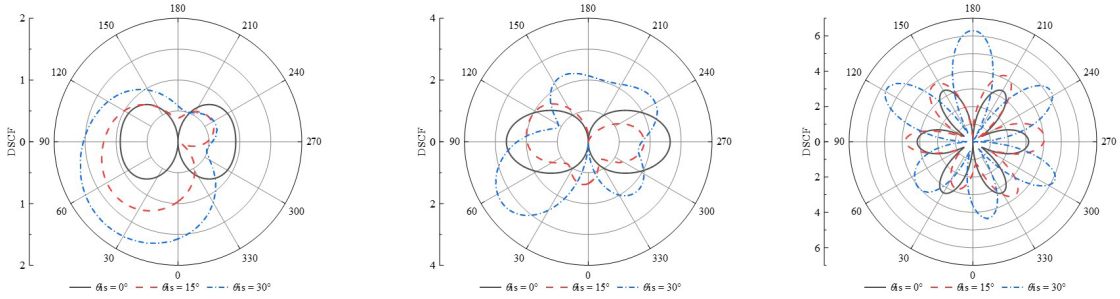

(a) η=0.5 (b) η=1.0 (c) η=2.0

Figure 5 Effect of incident angle on the DSCF of tunnel surface

4.2 *Influence of incident frequency*

Figure 6 shows the variation curves of displacements at the water-soil interface of dimensionless frequency for an SV wave incident at ϑ_{is} =30°. From Figure 6, it can be observed that the displacements at the water-soil interface vary significantly under different frequencies. As the incident wave frequency increases, the spatial distribution of displacement amplitude becomes more complex. On the incident wave side, the displacement distribution at the water-soil interface shows stronger spatial variations than the opposite side, with higher peak displacement amplitudes. The maximum displacement is also more frequently observed on the incident wave side. The tunnel reflects the wave on the incident side, causing wave energy to concentrate due to interference, leading to more complex displacements at the water-soil interface. On the opposite side, the tunnel shields the wave, weakening the oscillation and resulting in smaller displacement amplitudes, a result of the tunnel's filtering effect. These findings suggest that tunnel in high-frequency seismic events may experience concentrated stress and displacement on the incident side, which could impact the structural integrity and stability of underwater or underground tunnels. This highlights the importance of considering incident wave frequency in the seismic design of tunnels, as it directly affects the distribution displacement, especially in scenarios where complex wave interactions occur at the interface.

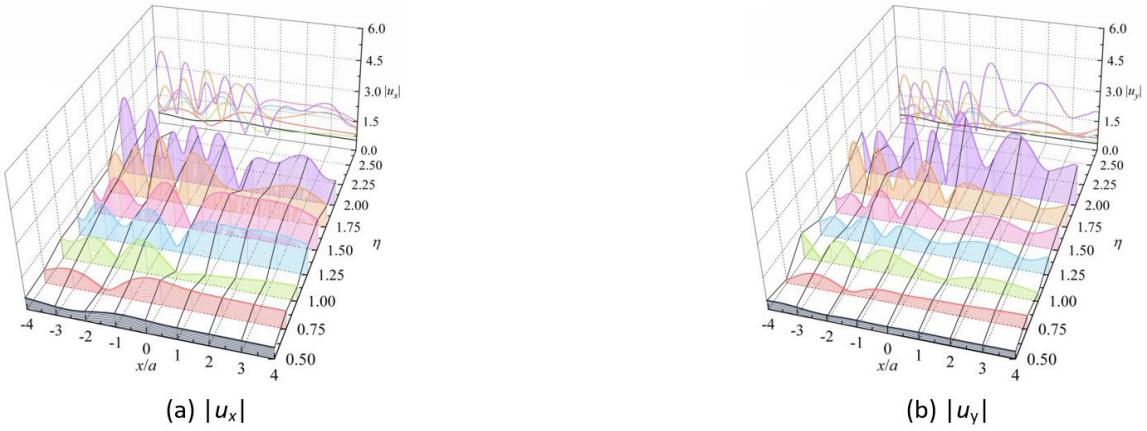

Figure 6 The curve of displacement distribution at the interface of water and soil with x/a and η change

4.3 *Influence of buried depth*

Figures 7 and 8 illustrate the variation curves of displacements at the water-soil interface, along with the DSCF distribution on the tunnel surface, for different burial depths (h/a=2, h/a=5, h/a=10) under SV wave incidence at dimensionless frequencies η=0.5, 1, and 2 and an angle of ϑ_{is} =30°. The corresponding burial depths represent shallow, reference, and deep burial conditions. Overall, under shallow burial conditions, the horizontal and vertical displacement distribution curves at the water-soil interface are relatively complex. At η=0.5, the horizontal displacement above the tunnel ($-1 \le x/a \le 1$) decreases as burial depth increases, whereas the vertical displacement increases. On the right side of the tunnel (x/a >1), both horizontal and vertical displacements at the water-soil interface decrease as the burial depth increases. This indicates that greater burial depth mitigates the displacement response, reducing the direct seismic impact on the tunnel. The deeper the tunnel, the more effective the soil's buffering effect becomes, diminishing wave-induced displacements. The DSCF on the tunnel surface reaches its maximum when the tunnel is deeply buried. Although deep burial reduces displacement, the increased stress concentration suggests that additional seismic design considerations are necessary to handle the amplified stresses at the tunnel walls. At η=1, the maximum displacements occur at h/a=5, near x/a =-1 and x/a =1. At this moment, the maximum dynamic stress concentration factor for deep burial occurs at the lower left of the tunnel (ϑ_1=60°). At a frequency of η=2, the maximum horizontal and vertical displacements under shallow burial conditions, as well as the maximum DSCF also occur at the top of the tunnel (ϑ_1=90°). This demonstrates that high-frequency waves induce pronounced stress concentrations and displacements at the tunnel crown in shallow burial conditions, which could lead to structural fatigue or failure over time. Therefore, for shallow tunnels, especially under high-frequency seismic wave exposure, strengthening the tunnel's crown is essential for seismic resilience.

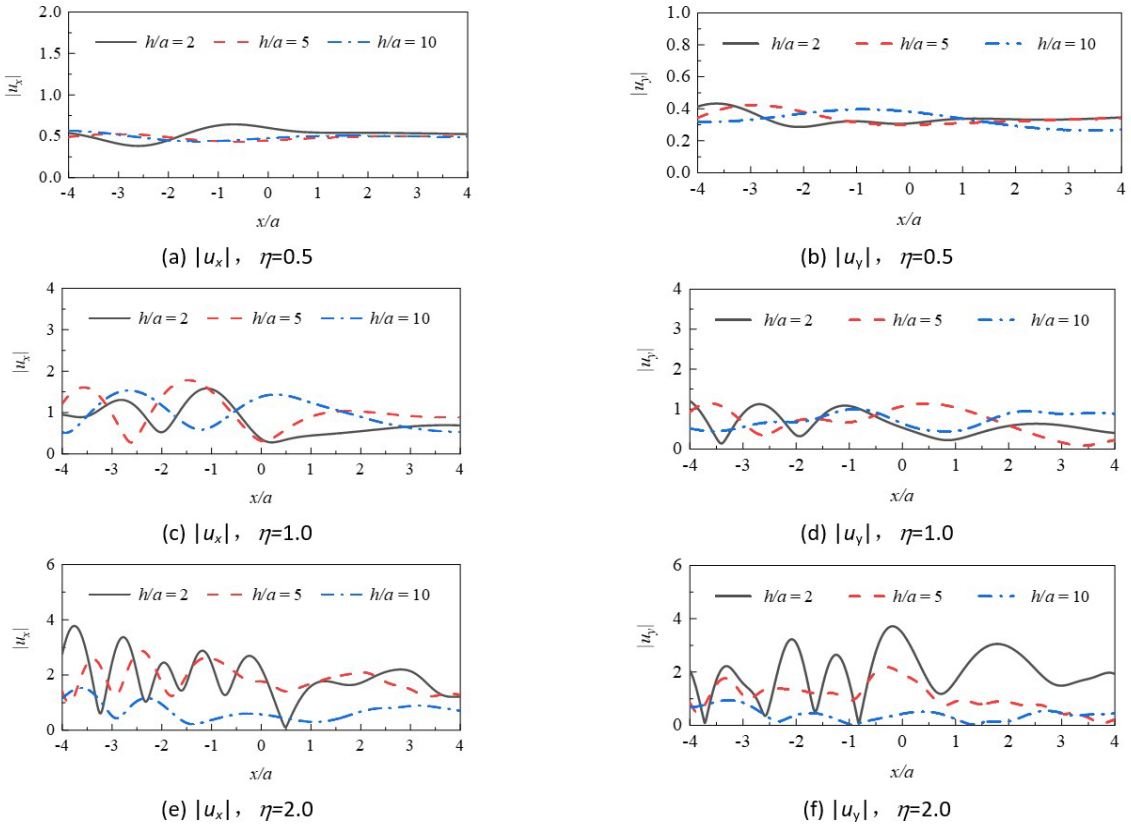

Figure 7 Effect of buried depth on the displacement

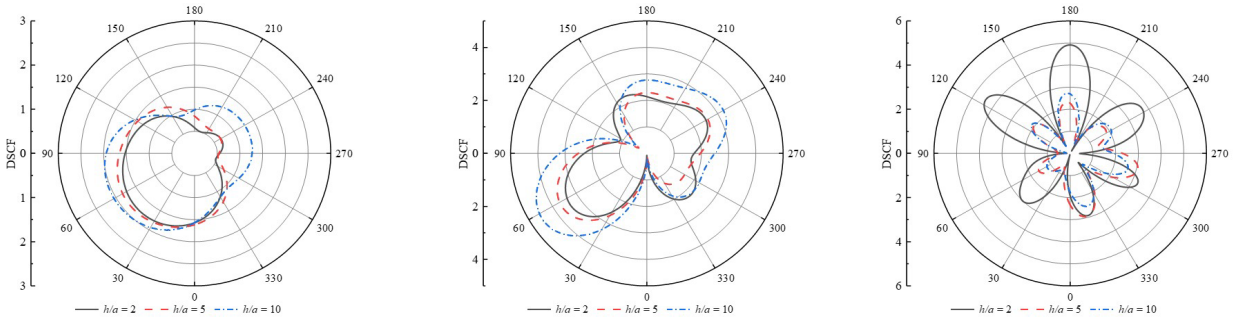

Figure 8 Effect of buried depth on DSCF of tunnel surface

4.4 *Influence of porosity*

Figures 9 and 10 show the variation curves of displacements at the water-soil interface and the DSCF distribution along the tunnel surface for different porosity conditions (n=0.1, n=0.2, n=0.4) under SV wave incidence with dimensionless frequencies η=0.5, 1, and 2 at an angle of ϑ_{is}=30°. The figures show that changes in porosity have a minimal effect on displacements at the water-soil interface, with similar horizontal and vertical displacement curves across porosity conditions. At η=0.5, horizontal displacement at the water-soil interface decreases while vertical displacement increases as porosity rises. This implies that structures such as tunnels situated in highly porous soils may experience stronger vertical seismic forces, which should be considered in design to mitigate potential vertical displacement damage. At η=1, horizontal and vertical displacements on the left side of the tunnel (x/a <1) decrease with increasing porosity, whereas on the right side (x/a >1), they increase. This suggests that porosity may cause uneven stress and displacement responses around tunnel structures, necessitating localized reinforcement in areas of high displacement. At η=2, displacements increase with porosity, with the effect being more pronounced on the right side of the tunnel (x/a >1). This highlights the need for additional seismic resilience in porous soils under high-frequency seismic waves, where the displacement impact becomes more critical. Figure 10 shows that the effect of porosity on DSCF varies with incident

frequency. At η=0.5 and 1, DSCF on the tunnel surface decreases with increasing porosity, but at η=2, it increases. This suggests that at lower frequencies, increased porosity reduces stress concentration on the tunnel, potentially lowering the risk of localized failure. However, at higher frequencies, increased porosity amplifies stress concentration on the tunnel surface, increasing the likelihood of structural damage.

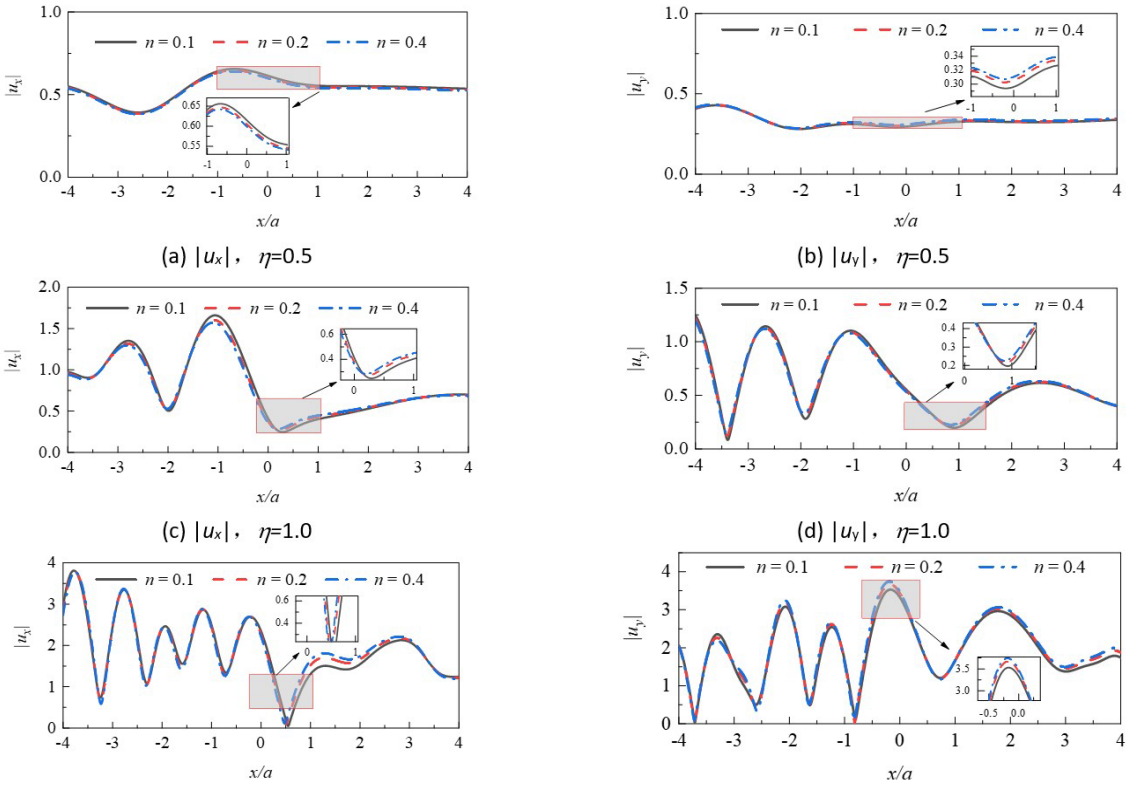

(a) $|u_x|$, η=0.5 (b) $|u_y|$, η=0.5

(c) $|u_x|$, η=1.0 (d) $|u_y|$, η=1.0

Figure 9 Effect of porosity on the displacement

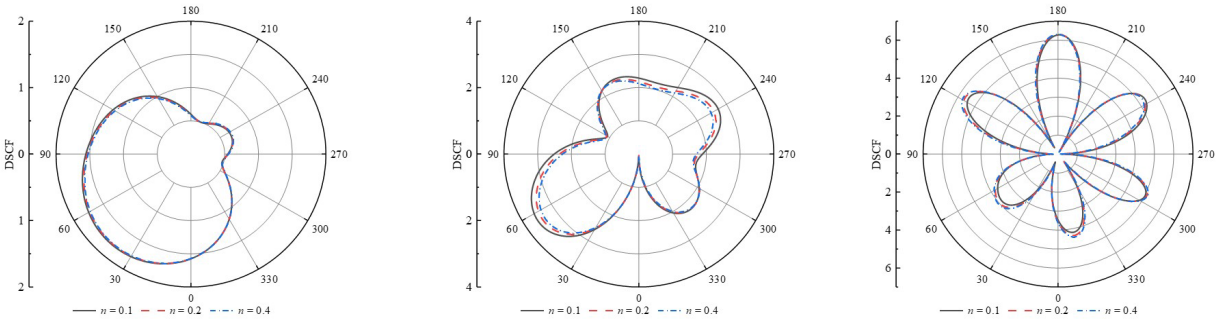

(a) η=0.5 (b) η=1.0 (c) η=2.0

Figure 10 Effect of porosity on DSCF of tunnel surface

5 Conclusions

This study applies wave theory of compressible ideal fluid media and Biot's theory of wave propagation in fluid-saturated media. Fluid-solid coupling in underwater saturated soil is considered, and the Fourier-Bessel series expansion method is used to derive an analytical solution for plane SV wave scattering around an unlined underwater tunnel. Numerical examples analyzed the effects of incident angle, frequency, buried depth, and porosity on displacements at the water-soil interface and DSCF on the tunnel surface. The conclusions are as follows:

(1) As the incident angle increases, horizontal displacement at the water-soil interface decreases, while vertical displacement increases. For vertical incidence ($\vartheta$is=0°), displacement and stress distributions at the water-soil interface and tunnel surface are symmetric. At an incident angle of 30°, DSCF on the tunnel surface reaches its maximum.

(2) As incident frequency increases, displacement distribution at the water-soil interface becomes more complex, with more pronounced peaks and troughs.

(3) In shallow burial conditions, horizontal displacement decreases with tunnel depth, while vertical displacement increases. In deep burial, maximum DSCF typically occurs at the lower left of the tunnel.

(4) At lower frequencies (η=0.5, 1), increasing porosity reduces horizontal displacement and DSCF at the water-soil interface. At higher frequencies (η=2), increasing porosity increases displacement and DSCF, especially on the right side of the tunnel.

The conclusions of this paper offer significant insights for the seismic design of traffic tunnels in saturated strata within high-seismic-intensity areas. The findings also provide useful references for the seismic design of underwater infrastructure, such as transmission pipelines, water conveyance systems, and oil pipelines. Future research should focus on the dynamic responses of underwater tunnels under the influence of complex seismic waves, especially considering the multi-wave coupling effects (Zhao et al., 2023b; Jiang et al., 2024) and thermal coupling effect (Yang et al., 2024). Additionally, it is necessary to further explore the seismic performance and potential damping measures for underwater tunnels subjected to oblique incidence of seismic waves, which can further enhance the resilience of these structures in real-world seismic conditions.

Acknowledgments

The authors express sincere thanks to the editors and anonymous reviewers for their constructive comments and suggestions that helped to improve the quality of this paper.

Author's Contributions: Conceptualization, Jia Ha and Guochao Li; Data curation, Jia Ha; Formal analysis, Guochao Li; Funding acquisition, Yanjun Fan; Investigation, Mingjian Yu; Methodology, Jia Ha; Project administration, Chong Niu; Resources, Guochao Li; Software, Mingjian Yu; Supervision, Chong Niu; Validation, Jia Ha, Guochao Li and Mingjian Yu; Visualization, Yanjun Fan; Writing – original draft, Jia Ha; Writing – review & editing, Guochao Li.

Editor: Rogério José Marczak

References

Pao, Y. H., Mow, C. C., Achenbach, J. D. (1973). Diffraction of elastic waves and dynamic stress concentrations. J Appl Mech 40(4), 213-219.

Lee, V. W., Trifunac, M. D. (1970). Response of Tunnels to Incident SH-Waves. J Engng Mech Div 105(4), 643-659.

Cao, H., Lee, V. W. (1979). Scattering and diffraction of plane P waves by circular cylindrical canyons with variable depth-to-width ratio. Soil Dyn Earthq Eng 9(3), 141-150.

Lee, V. W., Cao, H. (1989). Diffraction of SV by circular canyons of various depth. J. Eng. Mech. - ASCE 115(9), 2035-2056.

Todorovska, M. I. (1990). A note on response of shallow circular valleys to Rayleigh waves-analytical approach. Earthq. Eng. Eng. Vib 10, 21-34.

Todorovska, M. I., Lee, V. W. (1991). A note on scattering of Rayleigh waves by shallow circular canyons: analytical approach. Bull. Ind. Soc. Earth. Tech 28(2), 1-16.

Davis, C. A., Lee, V. W., Bardet, J. P. (2001). Transverse response of underground cavities and pipes to incident SV waves. Earthq. Eng. Struct. Dyn 30(3), 383-410.

Liang, J., Zhang, Y., Lee, V. W. (2005). Scattering of plane P waves by a semi-cylindrical hill: analytical solution. Earthq. Eng. Eng. Vib 4 (1), 27-36.

Liang, J., Zhang, H., Lee, V. W. (2003). A series solution for surface motion amplification due to underground twin tunnels: incident SV waves. Earthq. Eng. Eng. Vib (2), 289-298.

Liang, J.W., Zhang, H., Lee, V. W. (2004). An analytical solution for dynamic stress concentration of underground cavities under incident plane P waves. Chin. J. Geotech. Eng. (06), 815-819.

Zhang, Y., Zhang, N., Huang, C., et al. (2022). Effect of partially imperfect interface on dynamic response of a circular lined tunnel in an elastic half-space subjected to plane SH waves. Int. J. Geomech. 22(10), 04022165.

Liang, Y., Zhou, F., Cao, X., et al. (2023). Scattering of plane SH waves by a circular tunnel in nonlocal fractional-order viscoelastic half-space. Soil Dyn Earthq Eng. 170, 107934.

Zhao, M., de Oliveira Barbosa, J. M., Metrikine, A. V., et al. (2023a). Semi-analytical solution for the 3D response of a tunnel embedded in an elastic half-space subject to seismic waves. Soil Dyn Earthq Eng. 174, 108171.

Biot, M.A. (1956a). Theory of propagation of elastic waves in a fluid-saturated porous solid. I. low-frequency range. J Acoust Soc Am 28(2), 168-178.

Biot, M.A. (1956b). Theory of propagation of elastic waves in a fluid-saturated porous solid. II. Higher frequency range. J Acoust Soc Am 28(2), 179-191.

Zimmerman, C., Stern, M. (1993). Scattering of plane compressional waves by spherical inclusions in a poroelastic medium. J Acoust Soc Am 94(1), 527-536.

Senjuntichai, T., Rajapakse, R. (1993). Transient response of a circular cavity in a poroelastic medium. Int. J. Numer. Anal. Methods Geomech 17(6), 357-383.

Liang, J., Ba, Z., Lee, V. W. (2007a). Scattering of plane P waves around a cavity in poroelastic half-space (I): analytical solution. Earthq. Eng. Eng. Vib (01), 1-6.

Liang, J., Ba, Z., Lee, V. W. (2007b). Diffraction of plane SV waves by an underground circular cavity in a saturated poroelastic half-space. ISET J. Earthq 44 (2), 341-375.

Li, W. H., Zhao, C. G. (2004). An analytical solution for diffraction of plane P-waves by cylindrical cavity in a fluid-saturated porous media semi i-space. Rock Soil Mech. (12), 1867-1872.

Li, W.H., Zhao, C.G. (2008). An analytical solution for the scattering of plane SV-waves around cylindrical cavity in a fluid-saturated porous media half space. Earthq. Eng. Eng. Vib 28(06), 1-7.

Xu, C. J., Ding, H. B., Tong, L. H., et al. (2019). Scattering of a plane wave by shallow buried cylindrical lining in a poroelastic half-space. Appl. Math. Model.70, 171-189.

Liu, G., Li, X., Zhu, H. (2024). Plane SV-waves scattering by seawater convex surface topography and underlying lined tunnel in a saturated half-space. Soil Dyn Earthq Eng. 184, 108847.

Zhu, J., Kontoe, S., Li, X., et al. (2024). Ground motion amplification by twin circular tunnels for obliquely incident seismic waves: Effects of saturated poroelastic soil parameters. Soil Dyn Earthq Eng. 186, 108953.

Yuan, Z., Zheng, Y., He, J., et al. (2024). A comparison of two numerical models for modeling a twin tunnel in a saturated half-space. Eur. J. Environ. Civ. Eng. 1-25.

Huang, L., Liu, Z., Wu, C., et al. (2022). A three-dimensional indirect boundary integral equation method for the scattering of seismic waves in a poroelastic layered half-space. Eng. Anal. Bound. Elem 135, 167-181

Liu, Z., Liu, J., Meng, S., et al. (2021a). Diffraction of elastic waves by a fluid-filled crack in a fluid-saturated poroelastic half-space. Geophys J Int 225(3), 1530-1553.

Feng, G., Xie, L., Chow, Su. T. (2023). SV-wave scattering by an underwater circular cylindrical canyon in a saturated poroelastic half-space. Waves Random Complex Media 1-44.

Liu, G.H., Huang, W.W., Li, X. Y. (2021b). A theoretical solution for the scattering of incident plane P waves by a circular-arc site in saturated double-phase media with overlying water. Chin. J. Comput. Mech 38(2), 206-214.

Liu, G. H. Chen, X. Y., Li, X. Y. (2023). Theoretical solutions of variable seismic motions for scattering of incident P-waves by a medium-transition V-shaped canyon with partly filled water and its verification and characteristics. Chin. J. Comput. Mech 40(5), 764-772.

WANG, W. J. (1984). The waves in the viscous compressible fluid. Chin. J. Geophys 27(1), 87-96.

Zhou, F. X., Lai, Y. M., Song, R. X. (2013). Propagation characteristics of plane wave in non-homogeneously saturated soils. Sci. China Technol. Sci 43(2), 131-140.

Zhang, J. L., Ma, Q., Jiang, H. P. (2024). Study on the transmission and reflection of P1 wave at the interface between saturated soil and saturated frozen soil medium. Rock Soil Mech. (10), 1-14.

Ma, Q., Zhou, F., Shao, S., et al. (2023). Diffraction of plane P waves by a circular-arc canyon in an unsaturated poroelastic half-space. Soil Dyn Earthq Eng 174, 108163.

Liang, J. W., Yan, L. J., Lee, V. W. (2001). Effects of a covering layer in a circular-arc canyon on incident plane SV waves. Acta Seismol. Sin (06), 622-636.

Shi, T., Ma, Q., Zhang, M., et al. (2024). Scattering of plane P-waves by circular-arc canyon in saturated frozen soil half-space. Eng. Mech 1-21.

Zhao, S., Ma, Q. (2024). Diffraction of plane P waves by a circular unlined tunnel in an unsaturated poroelastic half-space. J. Vib. Eng. Technol 1-19.

Zhong, H., Zhang, Y. S. (2010). Broad-frequency-band analytical solution to scattering of plane SV wave by arc-shaped canyon topography. Earthq res China 26(02), 142-155.

Yang, C. H. (2009). Scattering of Plane P Wave in Circular-arc-shaped Canyon Topography: High-frequency Solution. Earthq res China 25(03), 234-245.

Liang, J., Liu, Z. (2009). Diffraction of plane SV waves by a cavity in poroelastic half-space. Earthq. Eng. Eng. Vib 8 (1), 29-46.

Liu, Z. J. (2015). Research on Wave Propagation Characteristics and Relevant Problems in Two-phase Porous Media. Zhejiang: Zhejiang University, China.

Zhao, M., Hu, S., Wang, P., et al. (2023b). Analysis of seawater-sediment-bedrock interaction model under obliquely incident P-SV waves with arbitrary angles. Appl. Ocean Res. 130, 103437.

Jiang, H., Ma, Q., Zhou, F., et al. (2024). Horizontal and vertical motion at the surface of seawater-gas hydrate bearing sediment-seabed under obliquely incident P waves. Appl. Ocean Res. 142, 103844.

Yang, Y., Ma, Q., Zhou, F. (2024). Seismic Response Study of S-Wave Incident Stratified Unsaturated Soil Site Under Thermal Effects. J. Earthq. Eng. 28(12), 3337–3362.